Supplementary Information (SI) for Nanoscale.
This journal is © The Royal Society of Chemistry 2025

Unveiling of free carrier transport and ion migration in 2D-3D perovskite mixture for stable optoelectronic devices

Bich Phuong Nguyen[1], Sarah Su-O Youn[2], Yeon Soo Kim[1], Thuy Thi Nguyen[1], Hakyung Park[2], Gee Yeong Kim[3] and William Jo[1,2]*

[1] New and Renewable Energy Research Center (NREC), Ewha Womans University, Seoul 03760, Republic of Korea

[2] Department of Physics, Ewha Womans University, Seoul 03760, Republic of Korea

[3] Advanced Photovoltaics Research Center, Korea Institute of Science and Technology (KIST), Seoul 02792, Republic of Korea

**Corresponding authors: William Jo (wmjo@ewha.ac.kr)*

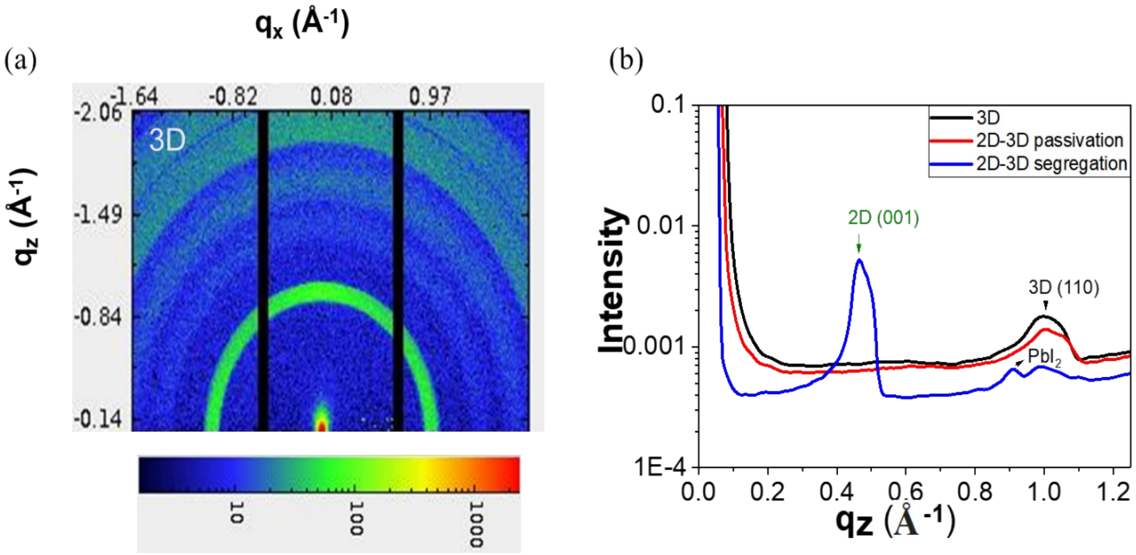

Figure S1. (a) GIWAXS images and schematics of pure 3D perovskite thin film under an incident beam angle of 0.2°. (b) Corresponding intensity profiles recorded along the q_z axis.

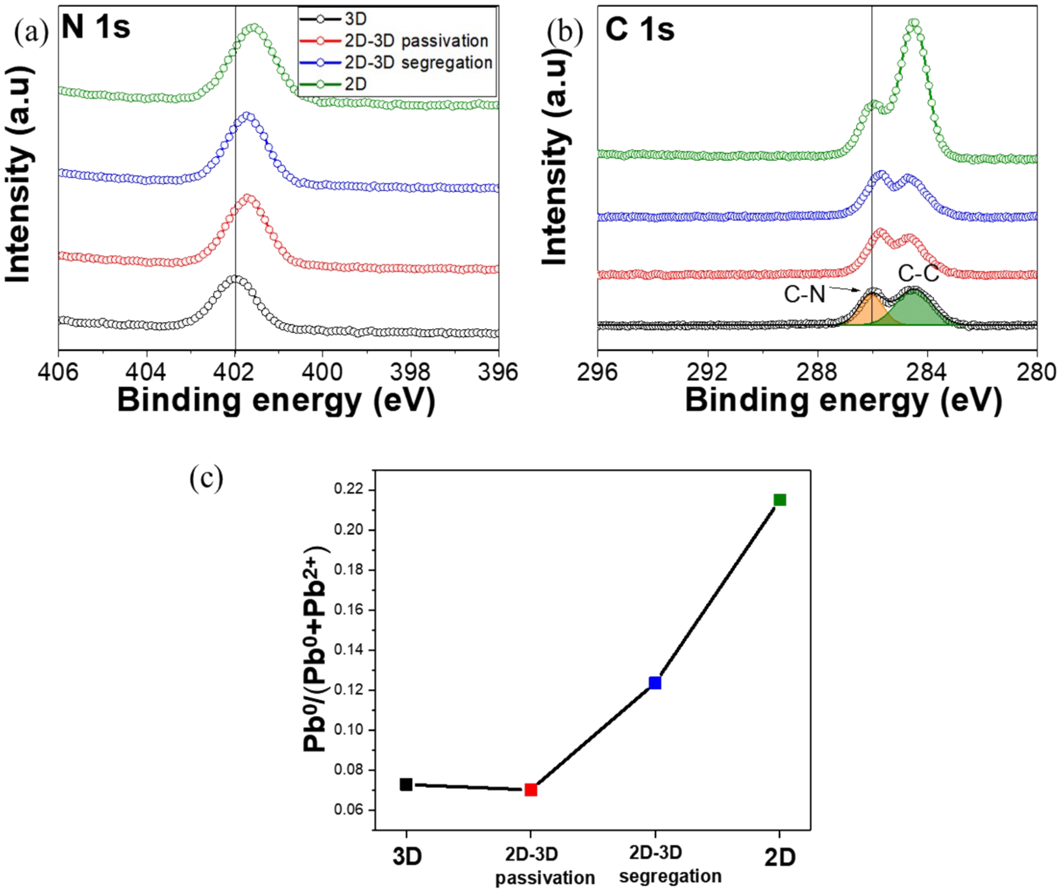

Figure S2. (a) N 1s core level XPS spectra and (b) C 1s core level XPS spectra for $(BA_2PbI_4)_x(MAPbI_3)_{1-x}$ perovskite films. (c) Fitted results for the $Pb^0/(Pb^0 + Pb^{2+})$ ratio.

The parameters of the vertical devices, like as the saturation current (I_0), and ideality factor (η) using the thermionic emission theory.[1] The Schottky diode current is expressed in the form

$$I = I_0 \left[exp\left(\frac{qV}{\eta KT}\right) - 1 \right] \tag{1}$$

$$I = AA^* T^2 exp\left(\frac{-q\varphi_b}{\eta KT}\right) \tag{2}$$

where, A, A^*, K, T, and q represent the effective diode area, Richardson's constant, the Boltzmann constant, temperature, and the charge of an electron, respectively.

Solving the above equation, the saturation current (I_0), and ideality factor (η) can be found using the following equations:

$$lnI = lnI_0 + \frac{qV}{\eta KT} \tag{3}$$

$$\eta = \frac{q}{mKT} \tag{4}$$

where the *m* and I_0 can be found from the slope and intercept of ln I vs V_f (forward voltage) plot (Figure S3).

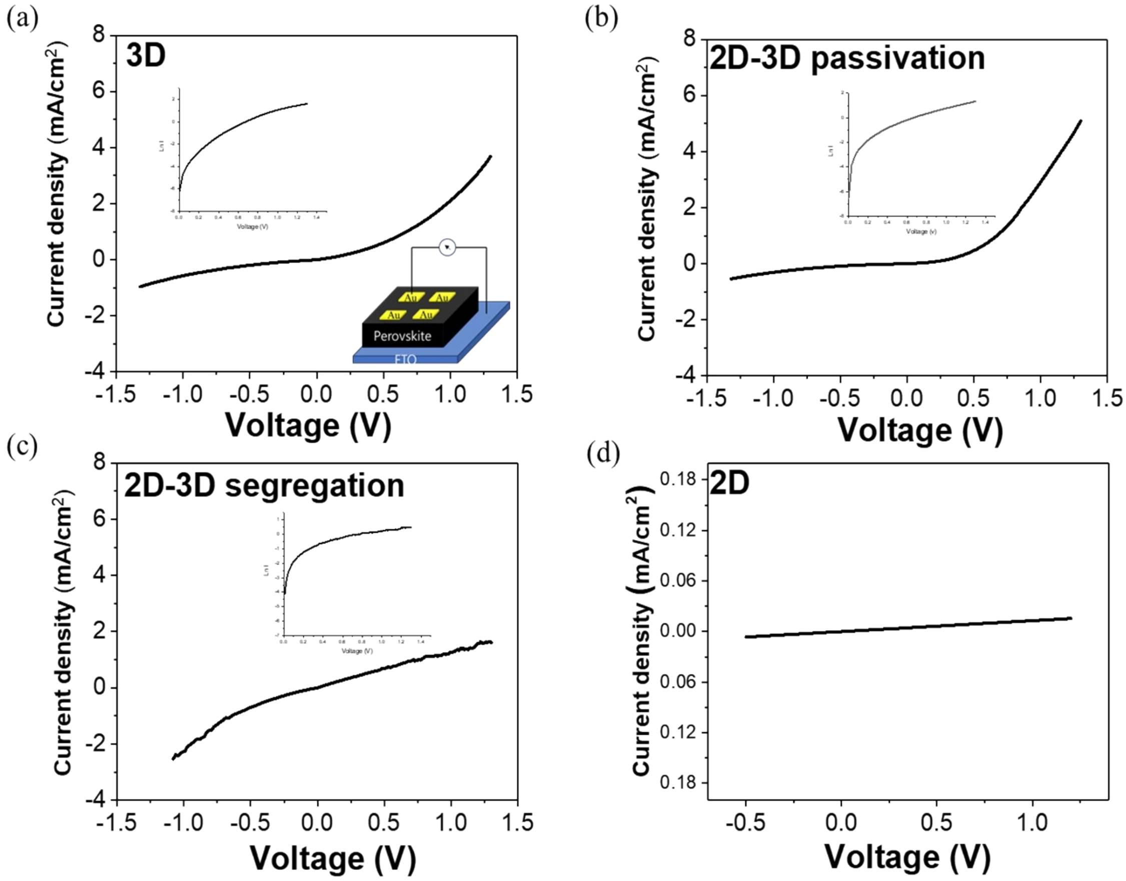

Figure S3. Room-temperature *J*–*V* curves recorded using the FTO/$(BA_2PbI_4)_x(MAPbI_3)_{1-x}$/Au device under dark condition and voltage ranging from − 0.5 V to 1.2 V. The inset depicts the semilogarithmic (Ln I vs V_f) plot and schematic of device.

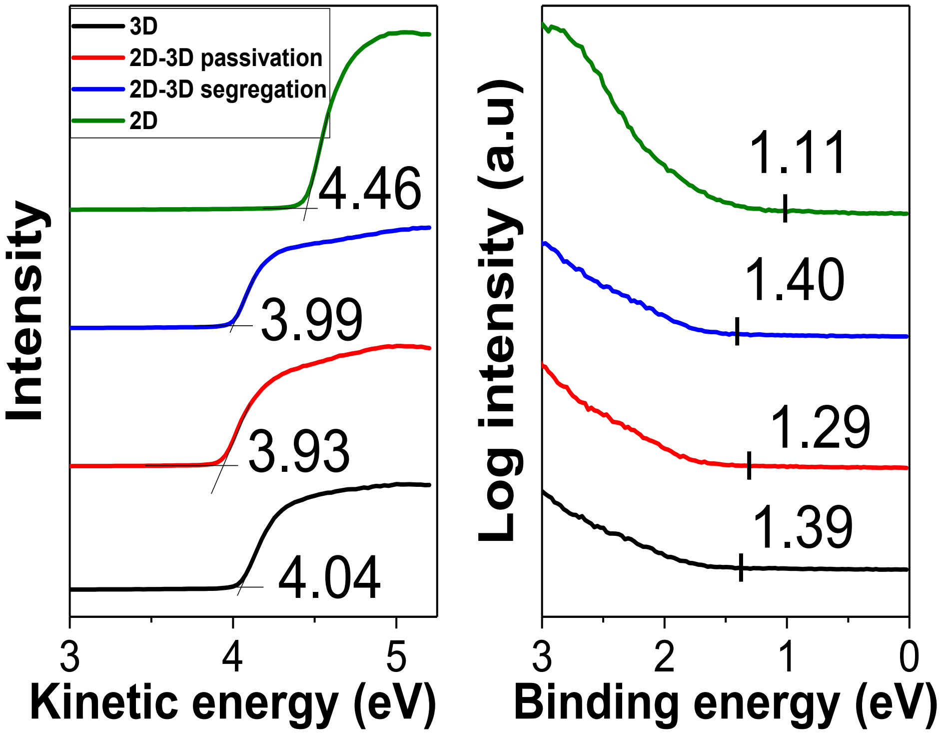

Figure S4. UPS curves, depicting the secondary electron cut-offs and valence bands of the $(BA_2PbI_4)_x(MAPbI_3)_{1-x}$ perovskite thin films.

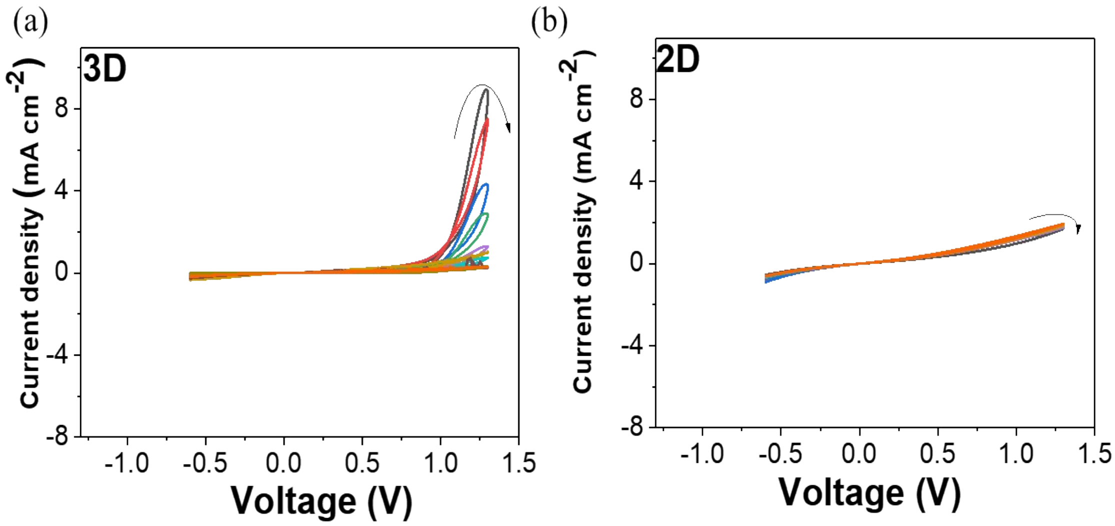

Figure S5. (a)–(b) Dark *J*–*V* curves of the 3D MAPbI$_3$ thin film, 2D, recorded at varying temperatures under a scan rate of 100 mV s^{-1} from − 0.5 V to 1.2 V and back to − 0.5 V.

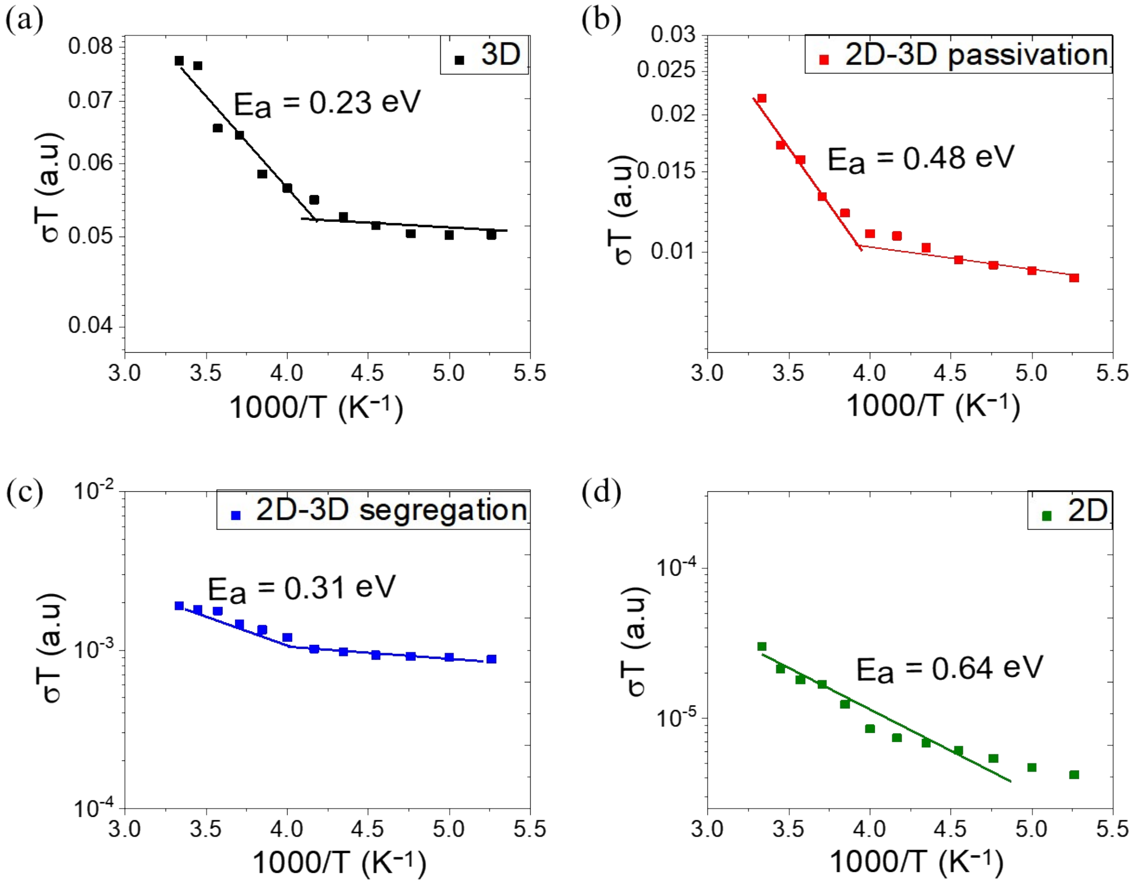

Figure S6. Fitted ion activation energies of the $(BA_2PbI_4)_x(MAPbI_3)_{1-x}$ thin films recorded by measuring their temperature dependent conductivity in the dark.

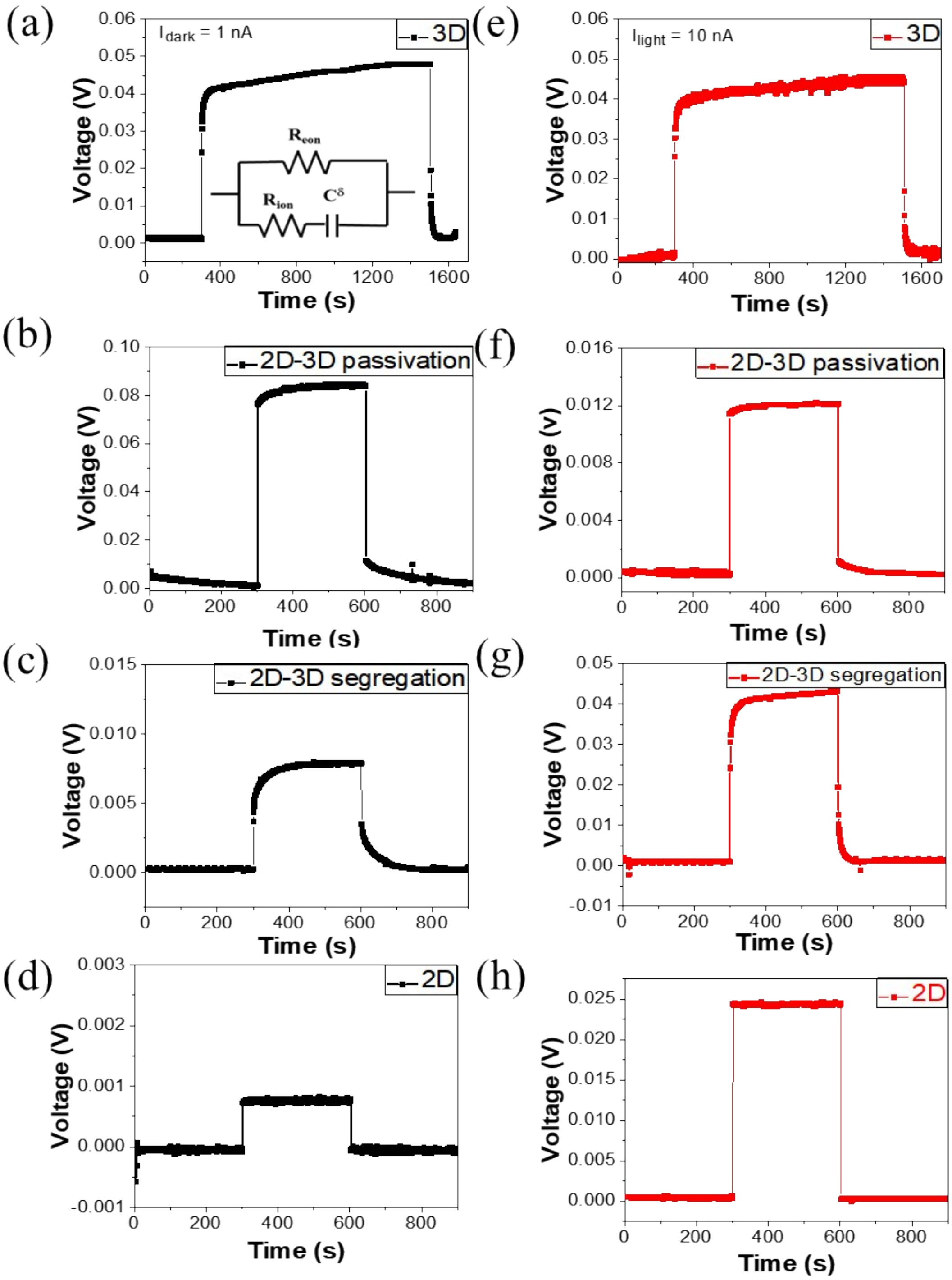

Figure S7. DC galvanostatic polarization curves of the $(BA_2PbI_4)_x(MAPbI_3)_{1-x}$ thin films recorded in an air atmosphere at room temperature: (a)–(d) Curves recorded in the dark under a constant current of 1 nA. The inset presents the equivalent circuit mimicking the galvanostatic characterization (R_{eon}: electronic resistance, R_{ion}: ionic resistance, C_{δ}: chemical capacitance). (b)–(h) Curves recorded under illumination and a constant current of 10 nA.

The chemical diffusion coefficient, D^{δ}, can be expressed as $D^{\delta} = \frac{L^2}{\pi^2 \tau^{\delta}}$, where L denoted the thickness of the sample, and τ^{δ} represents the polarization time constant. Generally, this chemical diffusion coefficient can be determined using two methods. The first method e analyzes the polarization transient based on short-time square-root-time behavior ($\sqrt{t}$). Meanwhile, the second method examines the observed, long-time exponential-time behavior. Figures S10 and S11 present polarization curves and time constant fitting under dark and illuminated condition, employing both the square root time behavior for short time and the long-time exponential behaviors. The time constants derived from the long-time fitting values align with the short-time fitting values (for more details regarding the technique, referred to literature[1] and references therein).

In term of DC polarization measurements, the chemical diffusion coefficient, D^{δ}, based on the long-time behavior is more reliable, as the results exclusively depend on a single parameter (i.e., the time constant). Conversely, the short-time behavior requires determination of the slope and voltage at the current interruption time (V_0), where experimental uncertainties in these two parameters can exert pronounced effects.

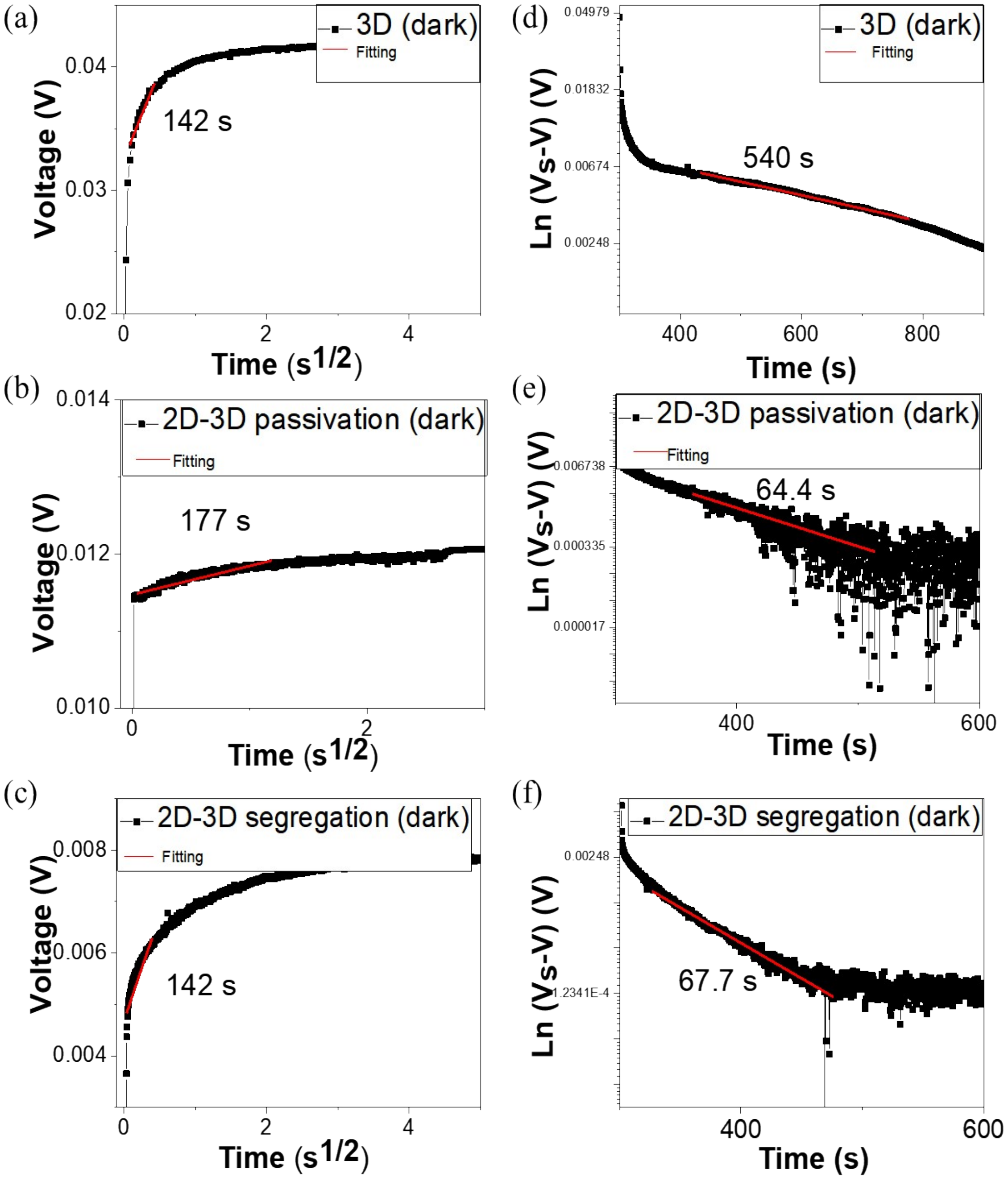

Figure S8. Stoichiometric polarization curves of the 3D $MAPbI_3$ and 2D–3D mixed perovskite thin films recorded in the dark and their fitting against short time (a)–(c) and long-time (d)–(f) behaviors.

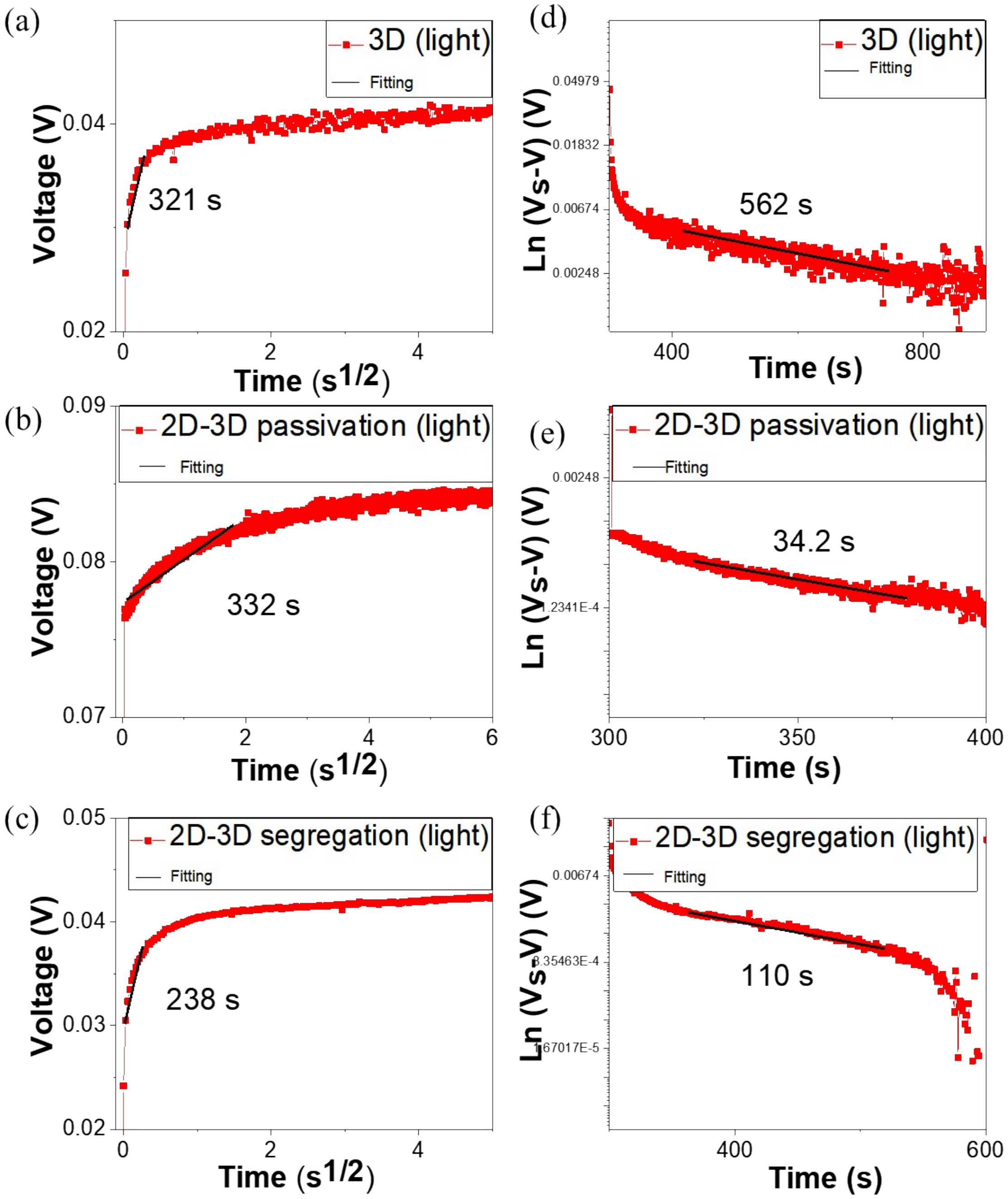

Figure S9. Stoichiometric polarization curves of the 3D MAPbI$_3$ and 2D–3D mixed perovskite thin films under illumination and their fitting against the short time (a)–(c) and long-time (d)–(f) behaviors.

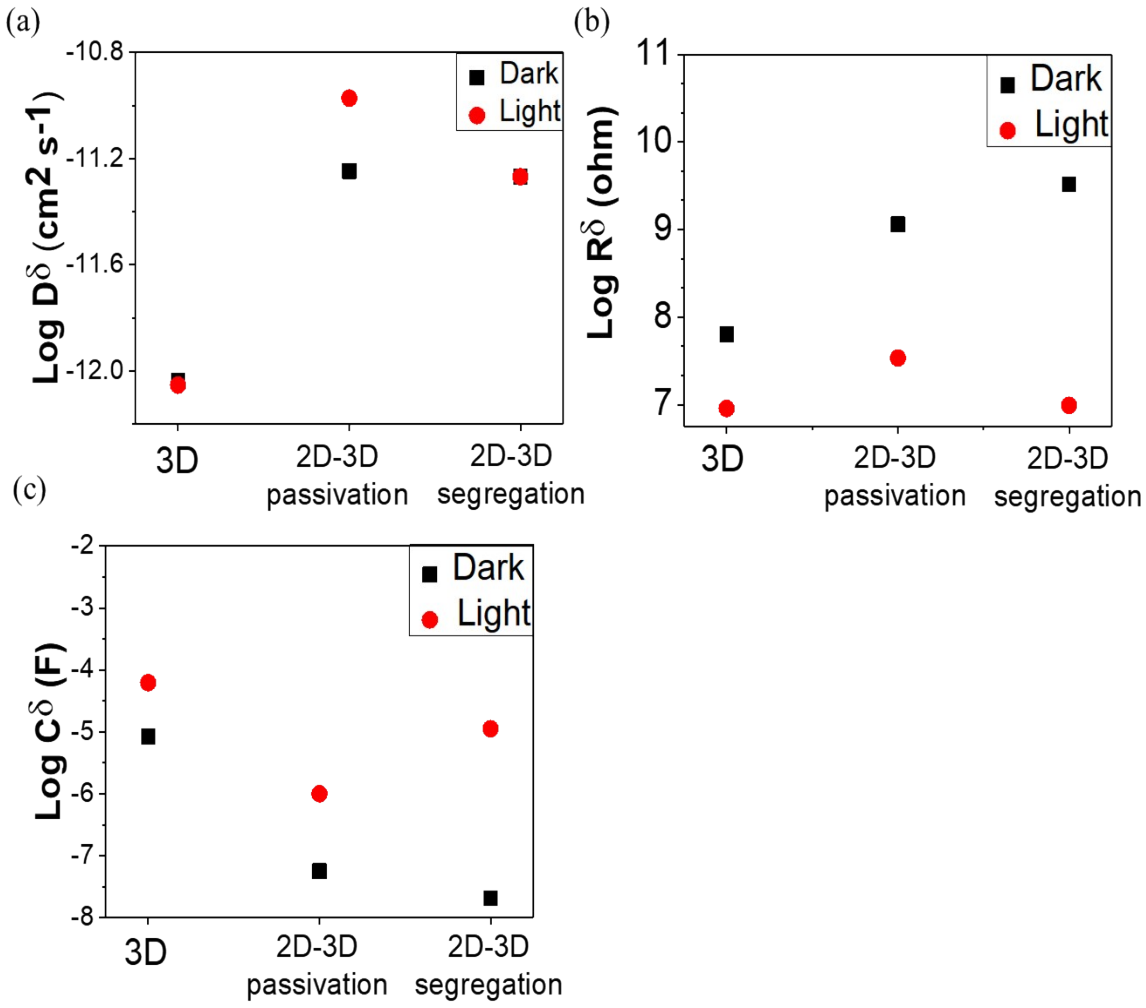

Figure S10. (a) Chemical diffusion coefficients of the 3D $MAPbI_3$ perovskite and 2D–3D mixed perovskites with different phases, recorded in the dark and under illumination. (b) Chemical capacitances (C^{δ}) and (c) resistances (R^{δ}) of the 3D $MAPbI_3$ and 2D–3D mixed perovskites recorded in the dark and under illumination. Notably, these chemical capacitances and resistances ($C^{\delta} = \iota^{\delta}/ R^{\delta}$) are calculated based on the electronic and ionic conductivities and the time constant. (c) Chemical diffusion coefficients of the 3D $MAPbI_3$ perovskite and 2D–3D mixed perovskites with different phases recorded in the dark and under illumination.

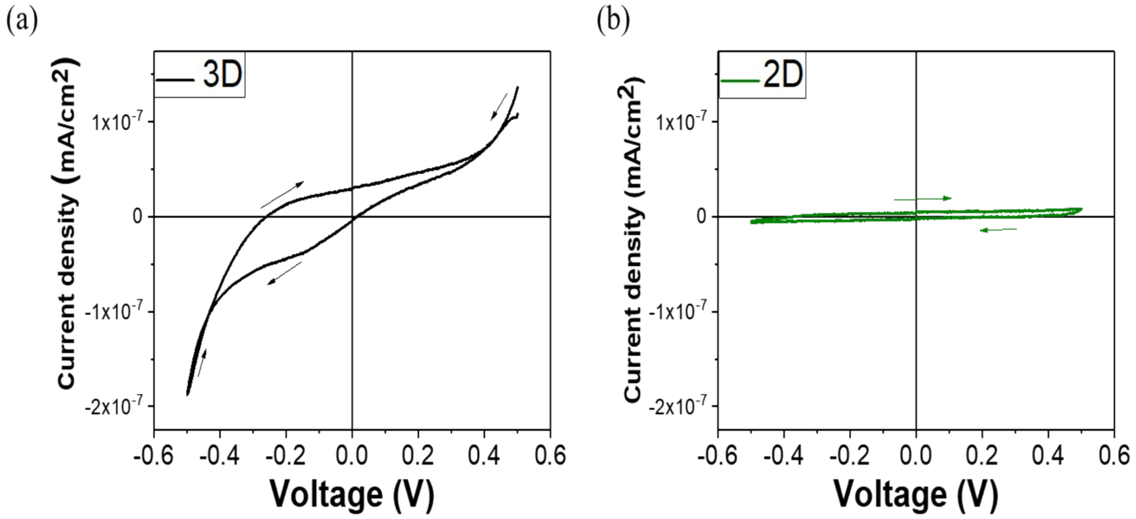

Figure 11. (a)–(b) Dark *J–V* curves of the 3D and 2D perovskite thin films deposited on the interdigital electrode arrays of gold structure, recorded at a scan rate of 100 mV s^{-1} from − 0.5 V to 0.5 V and back to − 0.5 V.

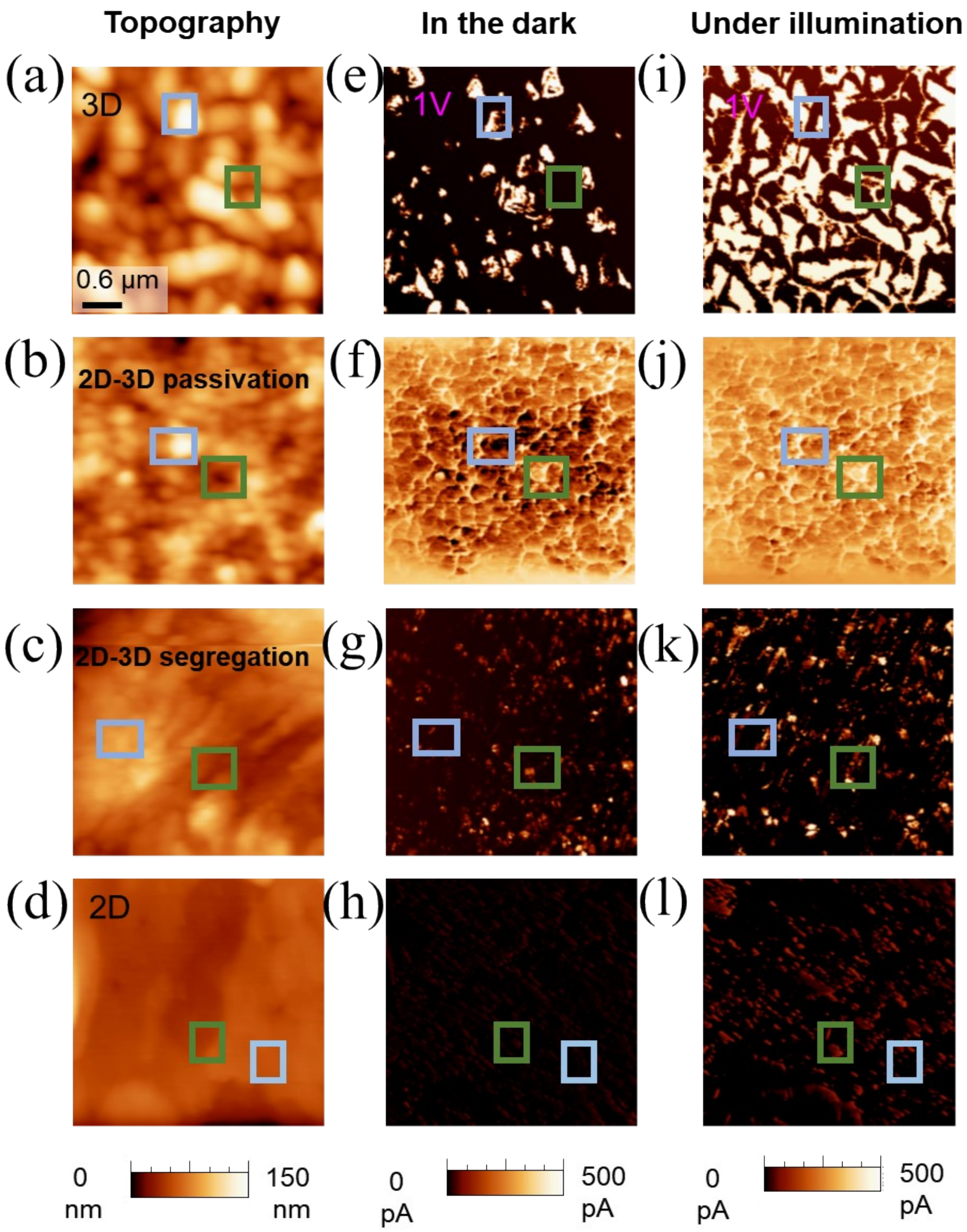

Figure S12. (a)–(d) Surface topography of the $(BA_2PbI_4)_x(MAPbI_3)_{1-x}$ thin films. (e)–(h) Corresponding C-AFM images recorded under a bias voltage of +1 V in the dark. (i)–(l) Corresponding C-AFM images recorded under a bias voltage of +1 V under illumination at 640 nm. The C-AFM tip was placed on the GB and IG regions indicated by blue and green rectangles, respectively.

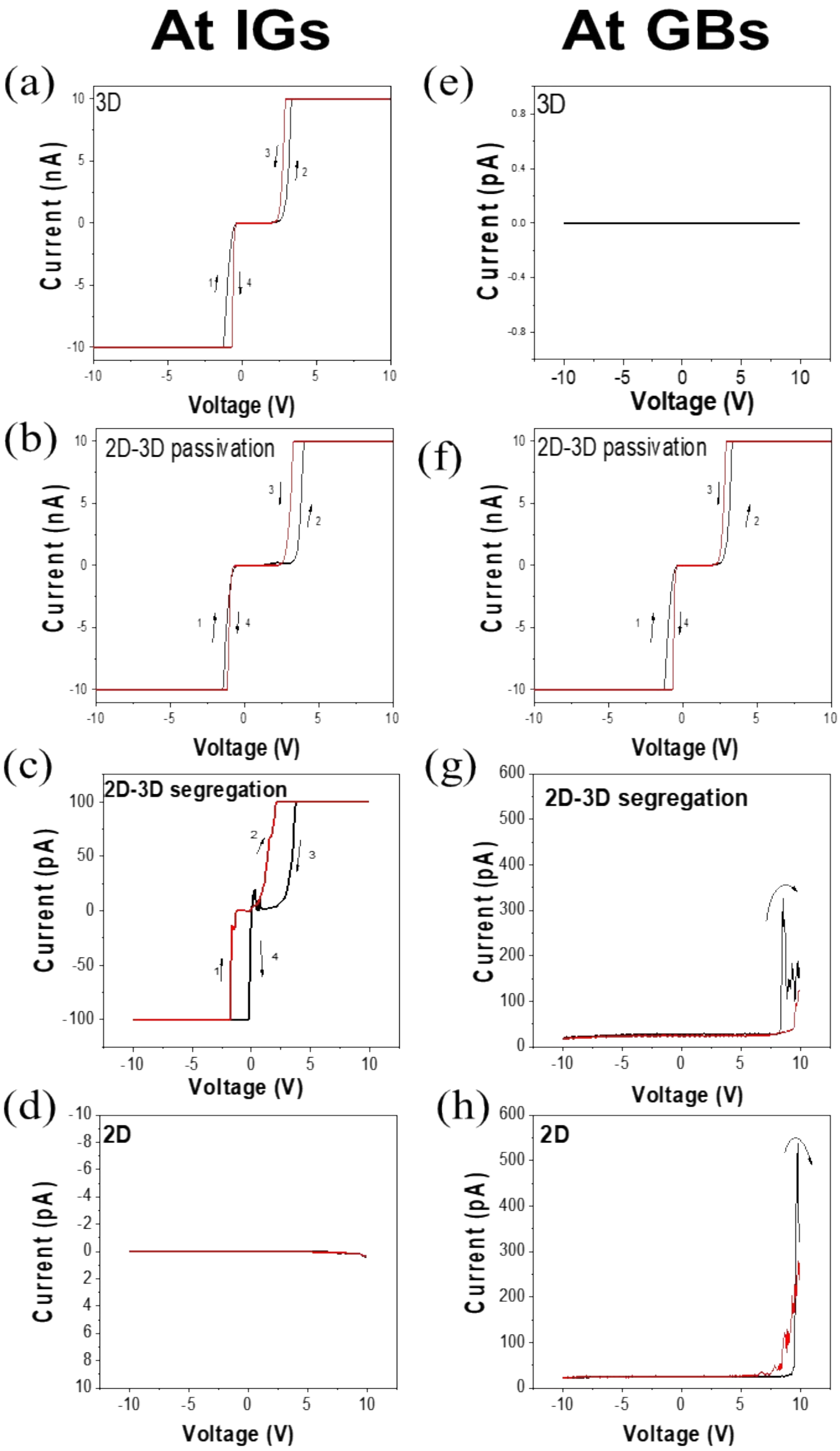

Figure S13. Single-point *I*–*V* curves extracted from the current mapping results derived from C-AFM measurements in the dark. Forward and reverse scanning *I*–*V* curves of the (a)–(d) $(BA_2PbI_4)_x(MAPbI_3)_{1-x}$ perovskite thin films at the GB and (e)–(h) at the IG.

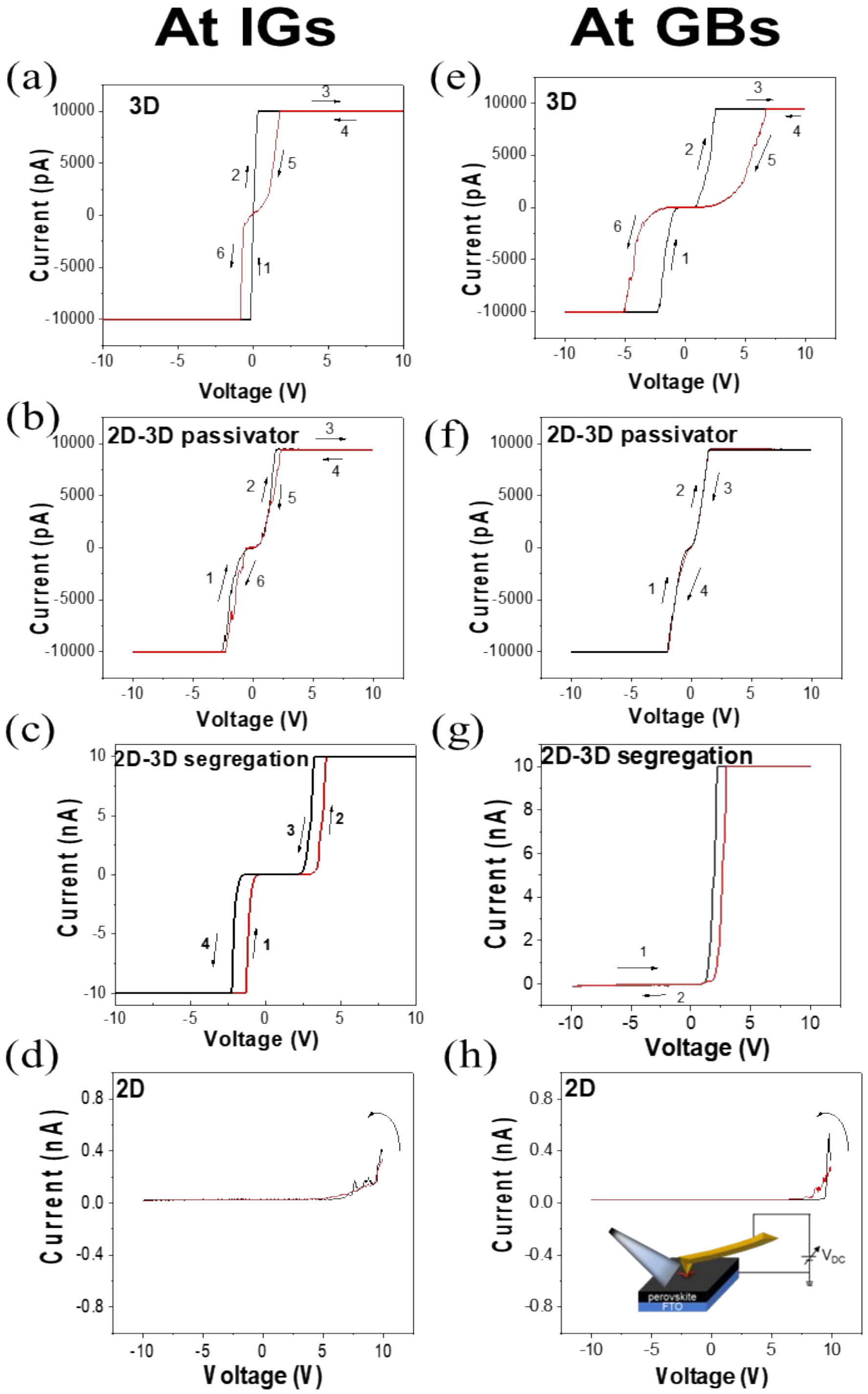

Figure S14. Single-point *I*–*V* curves extracted from the current mapping results derived from C-AFM measurements under illumination. Forward and reverse scanning *I*–*V* curves of the (a)–(d) $(BA_2PbI_4)_x(MAPbI_3)_{1-x}$ perovskite thin films at the GB and (e)–(h) at the IG. Also, the inset depicts the schematic C-AFM measurement setup.

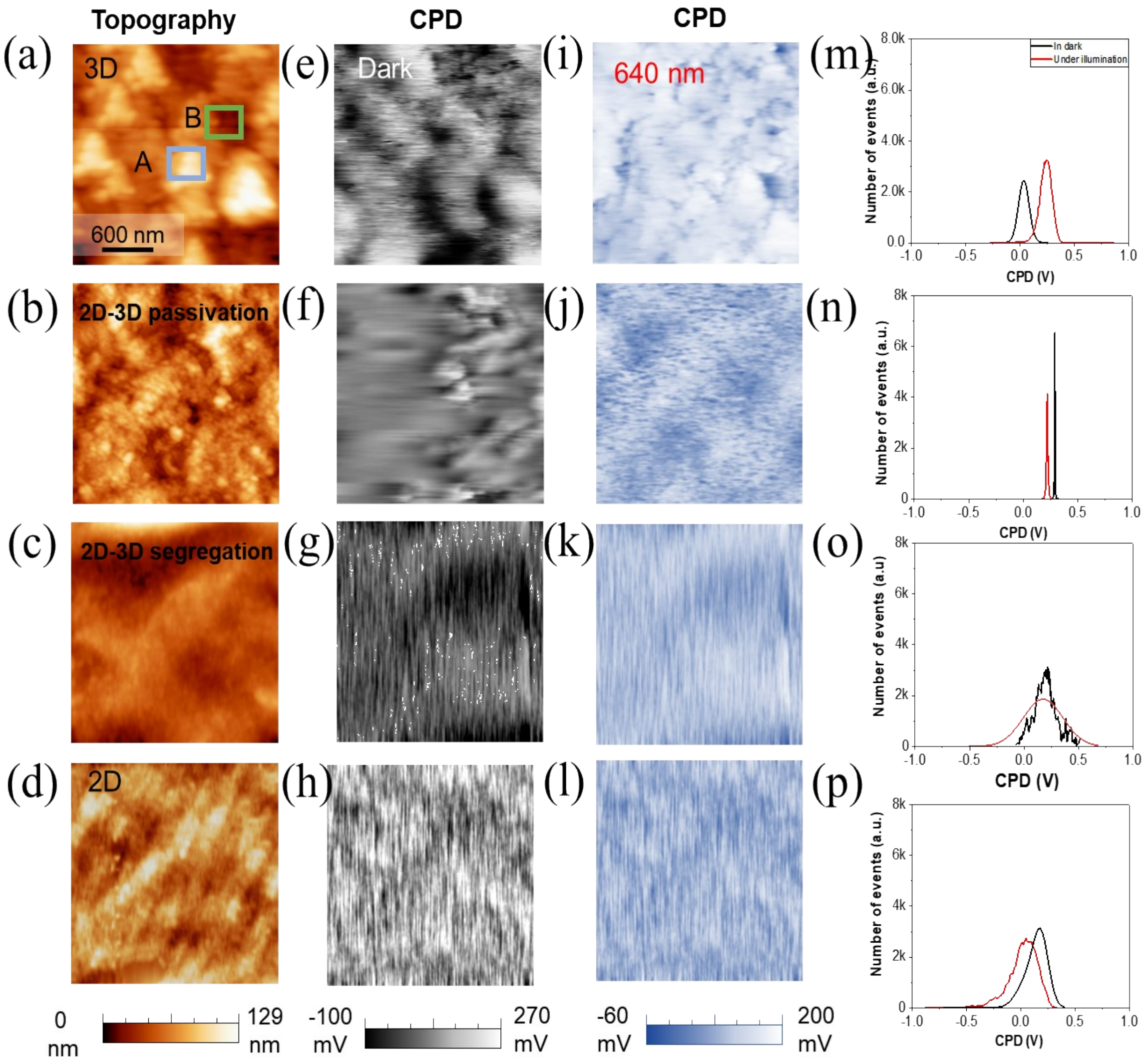

Figure S15. KPFM characterization: (a)–(d) Topographical images of the $(BA_2PbI_4)_x(MAPbI_3)_{1-x}$ perovskite thin films. (e)–(h) CPD maps in the dark. (i)–(l) CPD maps under illumination at 640 nm. (m)–(p) CPD distributions of the $(BA_2PbI_4)_x(MAPbI_3)_{1-x}$ films extracted from the KPFM images.

Reference

1. Sze, S. M.; Li, Y.; Ng, K. K., *Physics of semiconductor devices*. John wiley & sons: 2021.